

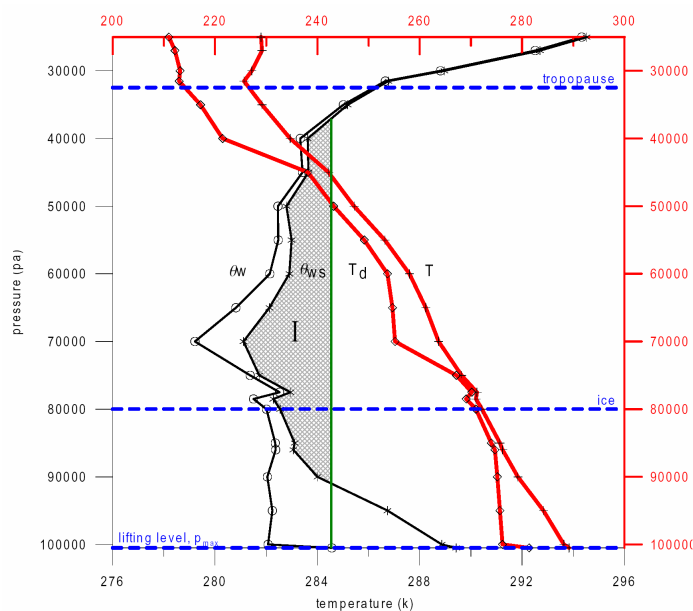
DANISH METEOROLOGICAL INSTITUTE

SCIENTIFIC REPORT

03-16

A generalized thunderstorm index developed for DMI-HIRLAM.

Niels Woetmann Nielsen
Claus Petersen



COPENHAGEN 2003

ISSN Nr. 0905-3263 (printed)
ISSN Nr. 1399-1949 (online)
ISBN-Nr. 87-7478-492-7

A generalized thunderstorm index developed for DMI-HIRLAM

Niels Woetmann Nielsen and Claus Petersen
Danish Meteorological Institute, Copenhagen, Denmark

Abstract

A generalized thunderstorm index based on parcel lifting from the lower and middle troposphere is described. The index requires calculation of tropopause pressure and vertical profiles of wet bulb potential temperature and wet bulb potential temperature at saturation. A simple method to estimate tropopause pressure from the vertical temperature profile is described and fast convergence iteration algorithms to calculate the wet bulb profiles are developed. Case studies indicate that the thunderstorm index performs better in mountain areas than the simpler K-index based on temperature and dew point temperature at fixed pressure levels. Over land without large mountains high values of the thunderstorm index tends to occur in regions that are more narrow than the regions of corresponding high values of the K-index. Over sea the opposite tends to be the case. However, the case studies do not provide reliable statistics to show whether the thunderstorm index generally performs better than the K-index. Extended-period verification with inclusion of lightning data is required to obtain more reliable statistics.

1. Introduction

It is of significant socio-economic value to be able to predict extreme weather such as severe winds, storm surges, heavy rain, extreme temperatures (including freezing temperature) and low visibility hours in advance. At least two lines of development can be followed. One is development of now-casting tools for these parameters. The second is development of prognostic or diagnostic extreme weather tools in a numerical weather prediction model or in a post processing step.

Now-casting of extremes aims at predicting them 3 to 6 hours in advance, while numerical models are more suitable beyond this range, although growing forecast errors resulting from analysis errors and model errors become of increasing concern as the forecasting lead time increases. The present report documents a generalized thunderstorm index developed for DMI-HIRLAM. The instability index displays regions of the troposphere with a high probability of thunderstorm developments.

The model performs a calculation of convective precipitation based on a parameterization scheme for convection. The intensity of convective precipitation in the model could therefore be used as an indicator of thunderstorms. The drawback is however, that such an indicator depends heavily on the applied convective parameterization scheme.

It was therefore decided to develop a generalized thunderstorm index that was not directly dependent on the convection scheme. This new instability index, which is based on calculation of tropospheric model profiles of wet bulb potential temperature (θ_w) and wet bulb potential temperature at saturation (θ_{ws}), is considered to be an alternative to simpler instability indices that have been widely used for a long time. The most commonly used simpler indices are the K-index, the lifted index, the Showalter index and the totals-totals index. The former three are based on parcel lifting from a specified pressure level in or near the top of the boundary layer to a specified pressure level in the upper-middle troposphere, typically 500 hPa. The totals-totals only makes use of temperature and dew point temperature at 850 hPa and temperature at 500 hPa (see for example Bluestein, 1993).

Section 2 contains a description of the new index, henceforth referred to as the θ_w -index. The index is based on vertical profiles of wet bulb temperature, wet bulb potential temperature and wet bulb potential temperature at saturation at the observed temperature. Fast iteration algorithms utilized to calculate these profiles are described in Appendix A-C. A description of a simple method to calculate the tropopause pressure from the vertical temperature profile is included in section 2. Examples of its performance are also shown. In section 3 the performance of the θ_w -index is compared with the performance of the simpler K-index in selected case studies. Finally, section 4 contains discussion and concluding remarks. Because of the considerable number of parameters that appears in the present report a list of symbols is given in Appendix D.

2. The θ_w -index

The calculation of the θ_w -index is done in five steps. In the first step the vertical profile of wet bulb temperature (T_w) is calculated. This profile is used in the second step as input to a first guess of θ_w in the calculation of the vertical θ_w profile. In the third step θ_w is used as input to the calculation of the vertical θ_{ws} profile. The tropopause pressure is calculated in the fourth step. Finally, in the fifth step the θ_w -index is calculated, making use of the previously calculated tropopause pressure and vertical profiles of θ_w and θ_{ws} . It turns out that a simple estimate of T_w can be used in the second step. Therefore the calculation of the T_w profile described in Appendix A is not a part of the generalized thunderstorm index. However, for the sake of completeness and because the T_w field may be useful in other applications we have included Appendix A in the present report.

2.1. Calculation of tropopause pressure

The vertical variation of θ_w and θ_{ws} in the stratosphere does not influence the instability index. Therefore the vertical profiles of θ_w and θ_{ws} are only calculated for the troposphere and lower stratosphere. Prior to the final calculation of the θ_w -index this procedure requires an estimate of the pressure p_T at the tropopause. This is not easily done unambiguously since ‘false’ tropopauses like sharp frontal zones and sharp inversions may be misinterpreted as the tropopause. The tropopause is calculated by going downward from the top of the model atmosphere, pressure level by pressure level. In each step the vertical temperature gradient $c = \partial T / \partial \ln p$ is calculated for 4 consecutive layers. The temperature gradients are compared with $c_0 = 38.2$ K, which is the gradient giving approximately a vertical temperature profile on a skew T- $\ln p$ diagram (e.g. Hess,

1966). First time the temperature gradient in the third of the four layers (from above) is larger than c_0 the tropopause pressure is calculated by log-linear interpolation of the temperature profiles in the first and third layer. If the second and third layer has a temperature gradient larger and smaller than c_0 , respectively, then the tropopause pressure is obtained by log-linear interpolation of the temperature profiles in the first and fourth layer. If no tropopause has been detected or the calculated tropopause is above 100 hPa the tropopause pressure is by default set to 100 hPa. Figure 1 shows examples of tropopause pressure in DMI-HIRLAM-E in a winter, spring, summer and autumn case. The tropopause pressure in this figure is calculated by utilizing the method described above. Generally there is good agreement between the calculated tropopause pressure and the tropopause pressure estimated from observed vertical profiles of temperature and dew point temperature. For the January case we compare the predicted tropopause pressure (Figure 1a) with two NOAA satellite images shown in Figure 2. The images were taken approximately at the verifying time of the forecast in Figure 1. The comparison shows qualitatively good correspondence between the predicted tropopause pressure and the cloud patterns shown by the satellite images. In the interpretation of the satellite images one should be aware of the following: Cold stratiform frontal clouds (white and relatively smooth) tend to be present on the anticyclonic shear side of upper-tropospheric jet streams with a downward sloping tropopause (increasing tropopause pressure) to the left of the flow direction. Polar tropospheric air tends to be capped by a relatively low tropopause. During winter convective clouds develop in cold polar air masses that are being advected over open sea. The convective clouds are often organized in open cells or cloud streets or in case of significant upper-level forcing in comma-shaped bands. Consequently, regions with these types of clouds over open sea and downstream coastal land, are likely to have a relatively low tropopause.

Note that the predicted high tropopause pressure southwest of Iceland and northwest of Portugal/Spain (Figure 1a) both are regions where the satellite image (Figure 2, left) shows convective clouds organized in open cells and comma clouds. Note also that the comma cloud system over Denmark (Figure 2, right) coincides with an area of high tropopause pressure predicted by DMI-HIRLAM-E (Figure 1a). Heavy snowfall was produced by this cloud system. In the Copenhagen-area the ground became covered with about 40 cm of snow.

Over wintertime continents the relationship described above between high tropopause pressure and convective clouds does not exist. The high tropopause pressure predicted over the western part of Russia must therefore be verified by other means. Temperature soundings at 00 UTC on 6 January indicate tropopause pressure down to 500 hPa in this area (figure not shown), which is in good agreement with the predicted tropopause pressure.

2.2. The generalized thunderstorm index

The θ_w -index is based on parcel lifting from levels with a pressure larger than $p_c = p_s - a_p(p_s - p_T)$. In the latter expression p_c is a "critical" pressure level above which parcel lifting is unlikely to generate thunderstorms, p_s is the surface pressure and p_T is the tropopause pressure. Presently $a_p = 0.6$.

For each lifting level p_i , $i=1,..,k$, the vertical integral from p_i to the pressure level

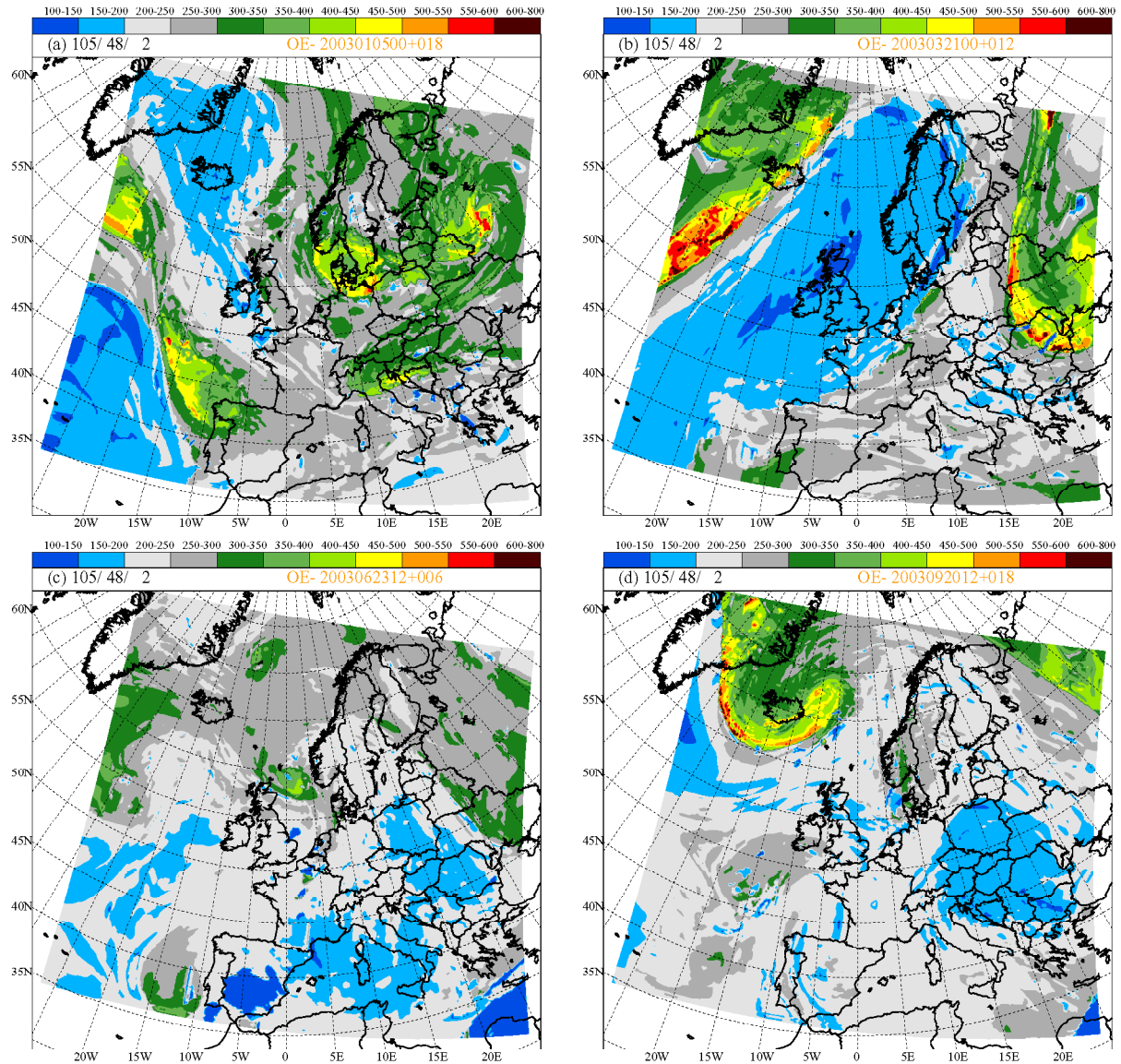


Figure 1: DMI-HIRLAM-E forecasts of the tropopause in hPa for (a): a winter case (18 hour forecast from 00 UTC 5 January 2003), (b): a spring case (12 hour forecast from 00 UTC 21 March 2003), a summer case (6 hour forecast from 12 UTC 23 June 2003) and an autumn case (18 hour forecast from 00 UTC 20 September 2003)

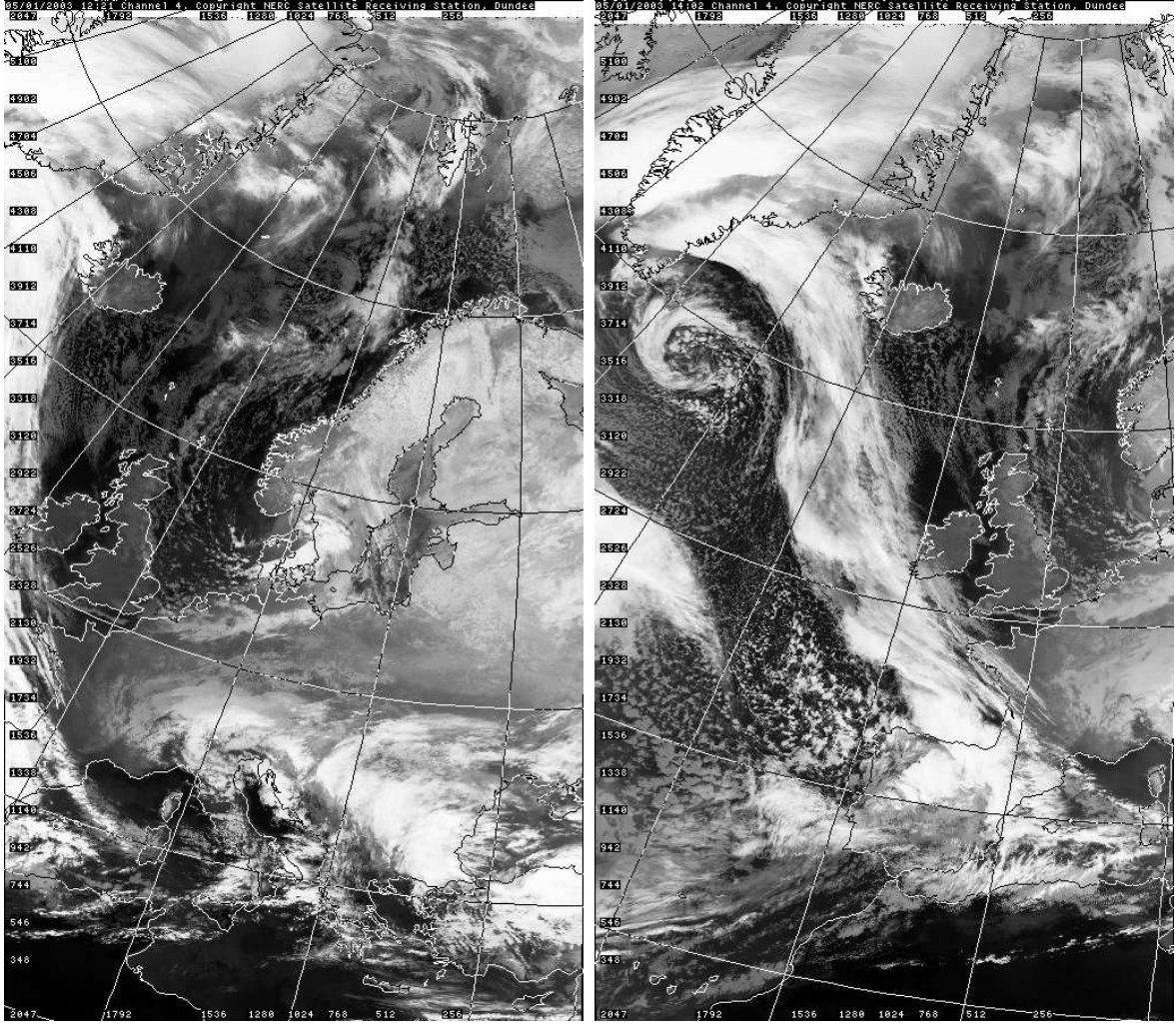


Figure 2: NOAA infrared satellite images. Left: 12.21 UTC 5 January 2003 and right: 14.02 UTC 5 January 2003.

p_{imax} of the difference $\theta_w^p(p_i) - \theta_{ws}^e(p)$ is calculated. Here k is the number of lifting levels, $\theta_w^p(p_i)$ is the wet bulb potential temperature of the parcel, $\theta_{ws}^e(p)$ is the saturation wet bulb potential temperature of the environment and p_{imax} is the pressure level above p_i , where

$$I_i(p) = - \int_{p_i}^p (\theta_w^p(p_i) - \theta_{ws}^e(p')) \cdot dp' \quad (1)$$

has its maximum value

$$I_{imax} = - \int_{p_i}^{p_{imax}} (\theta_w^p(p_i) - \theta_{ws}^e(p')) \cdot dp'. \quad (2)$$

The procedure is illustrated schematically in Figure 6. The maximum value I_{max} of I_{imax} , $i=1, \dots, k$, is determined together with the corresponding lifting pressure level p_{max} and the pressure level p_b . The latter is the first pressure level above p_{max} , where

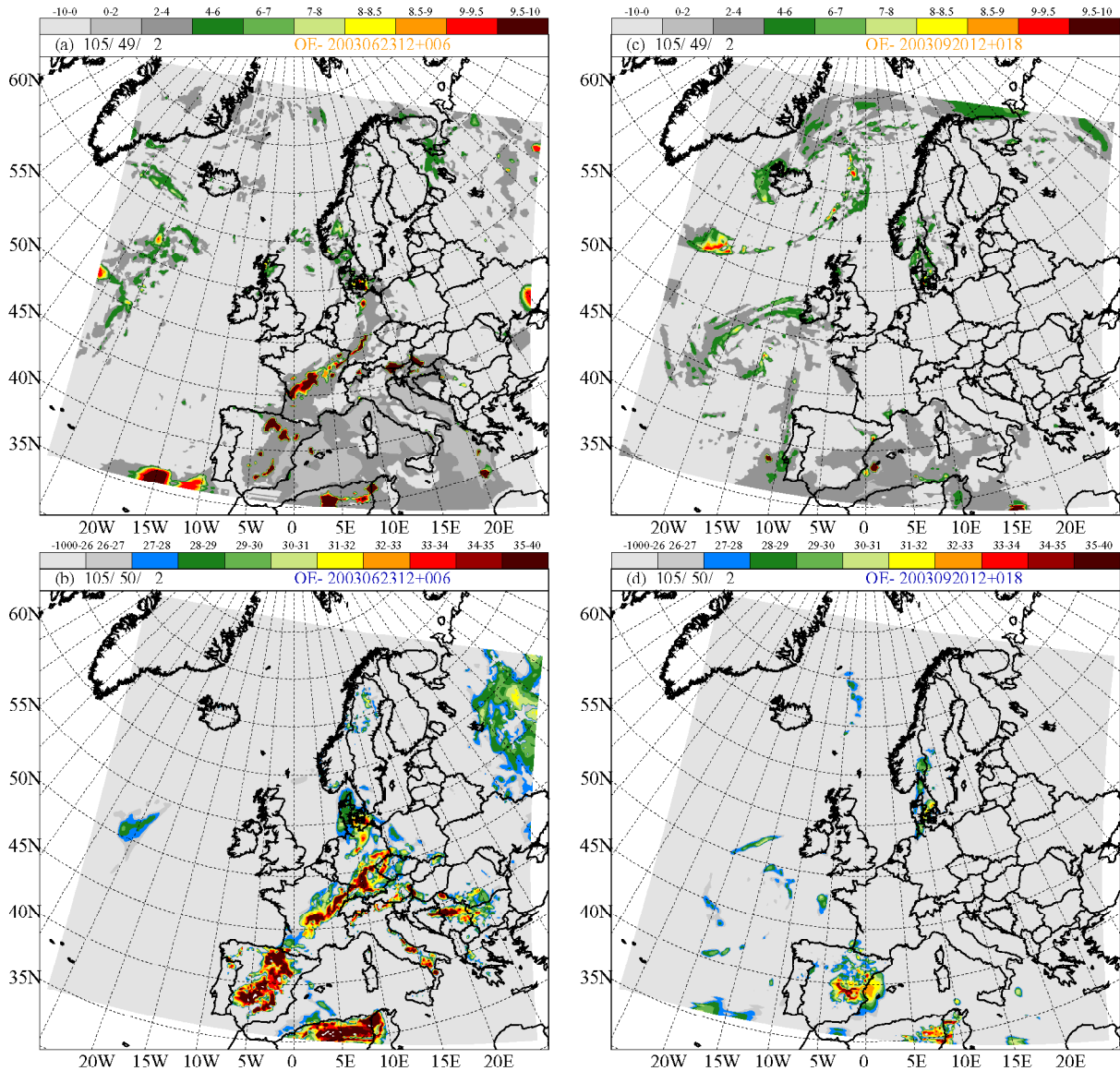


Figure 3: Top row: DMI-HIRLAM-E forecasts of the θ_w -index (nondimensional) for left: 23 June 2003 (6 hour forecast from 12 UTC 23 June) and right: 21 September 2003 (18 hour forecast from 12 UTC 20 September). Bottom row: DMI-HIRLAM-E forecasts of the K-index (unit K) for left: 23 June 2003 (6 hour forecast from 12 UTC 23 June) and right: 21 September 2003 (18 hour forecast from 12 UTC 20 September).

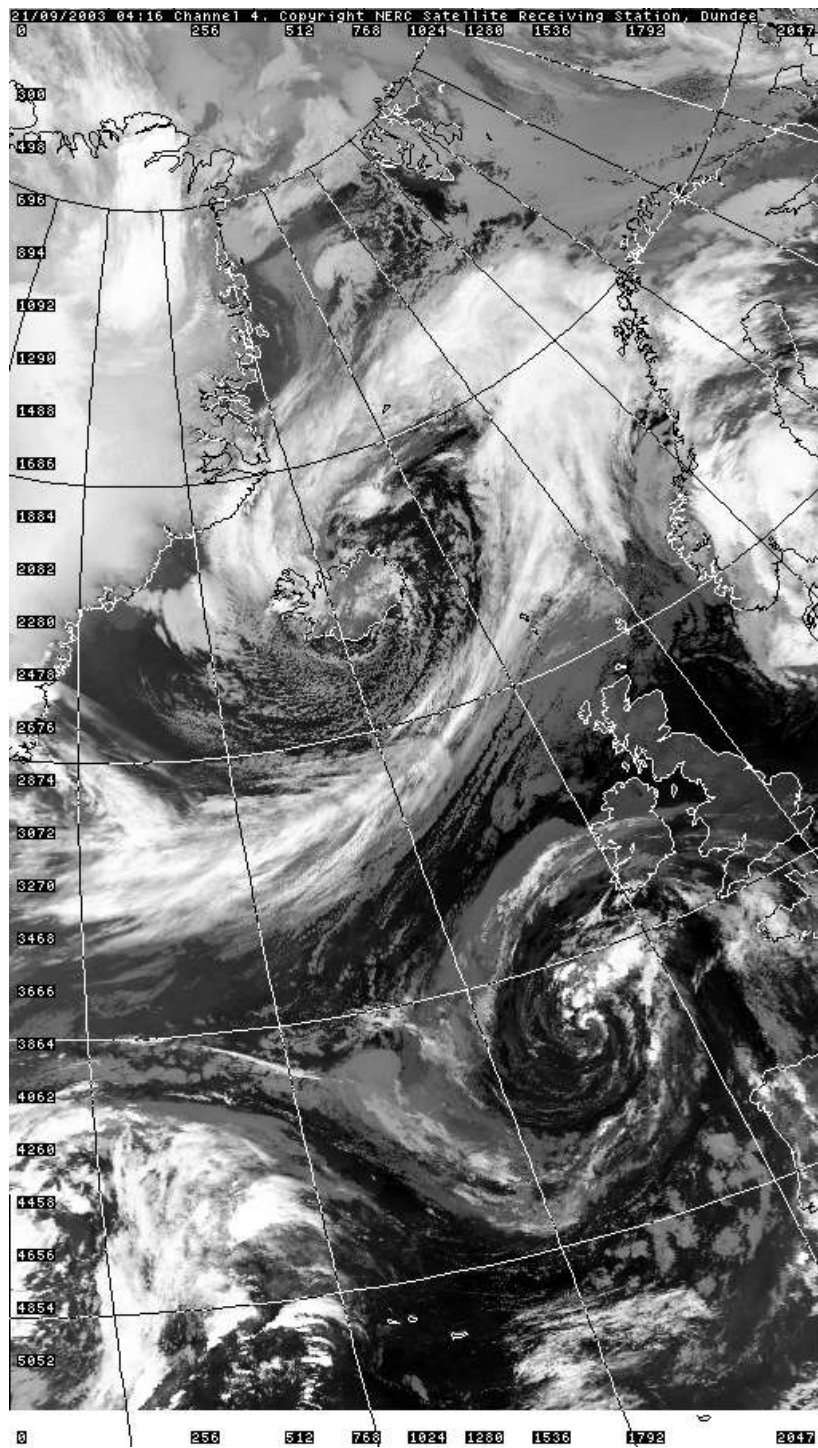
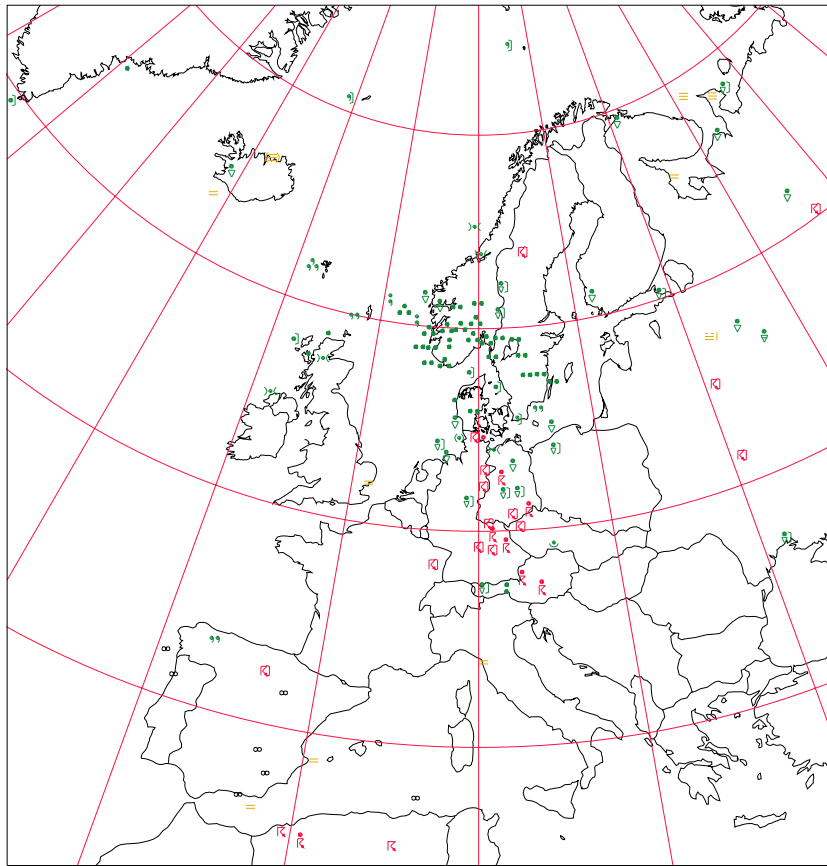
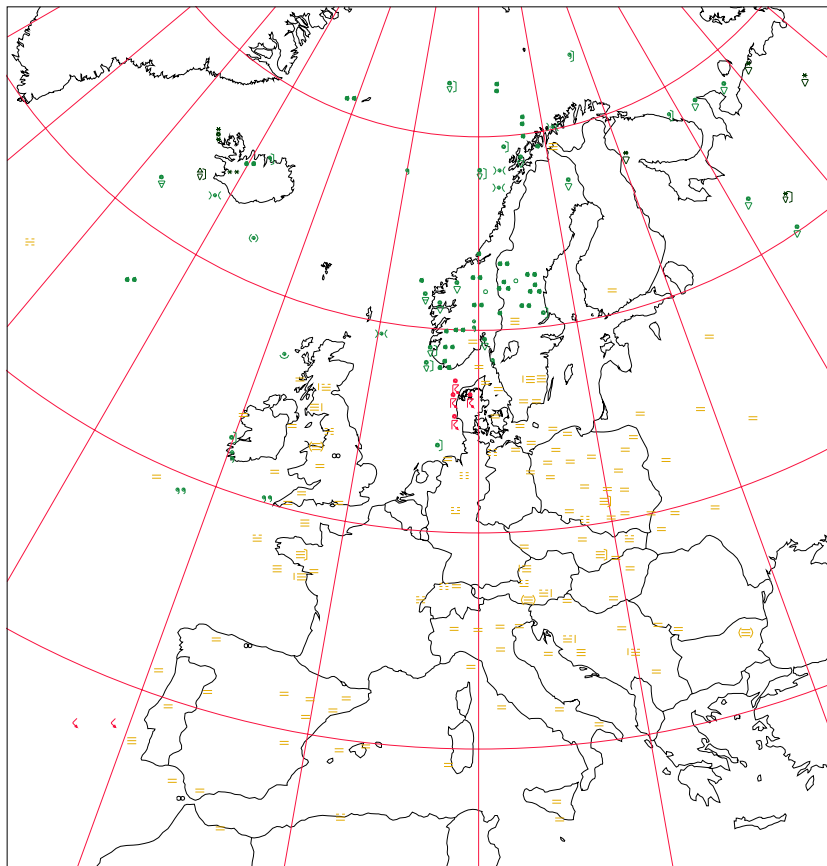


Figure 4: NOAA infrared image from 04.16 UTC 21 September 2003.



(a)



(b)

Figure 5: Synop observations of 'weather'. Top: 18 UTC 23 June 2003. Bottom: 06 UTC 21 September 2003.

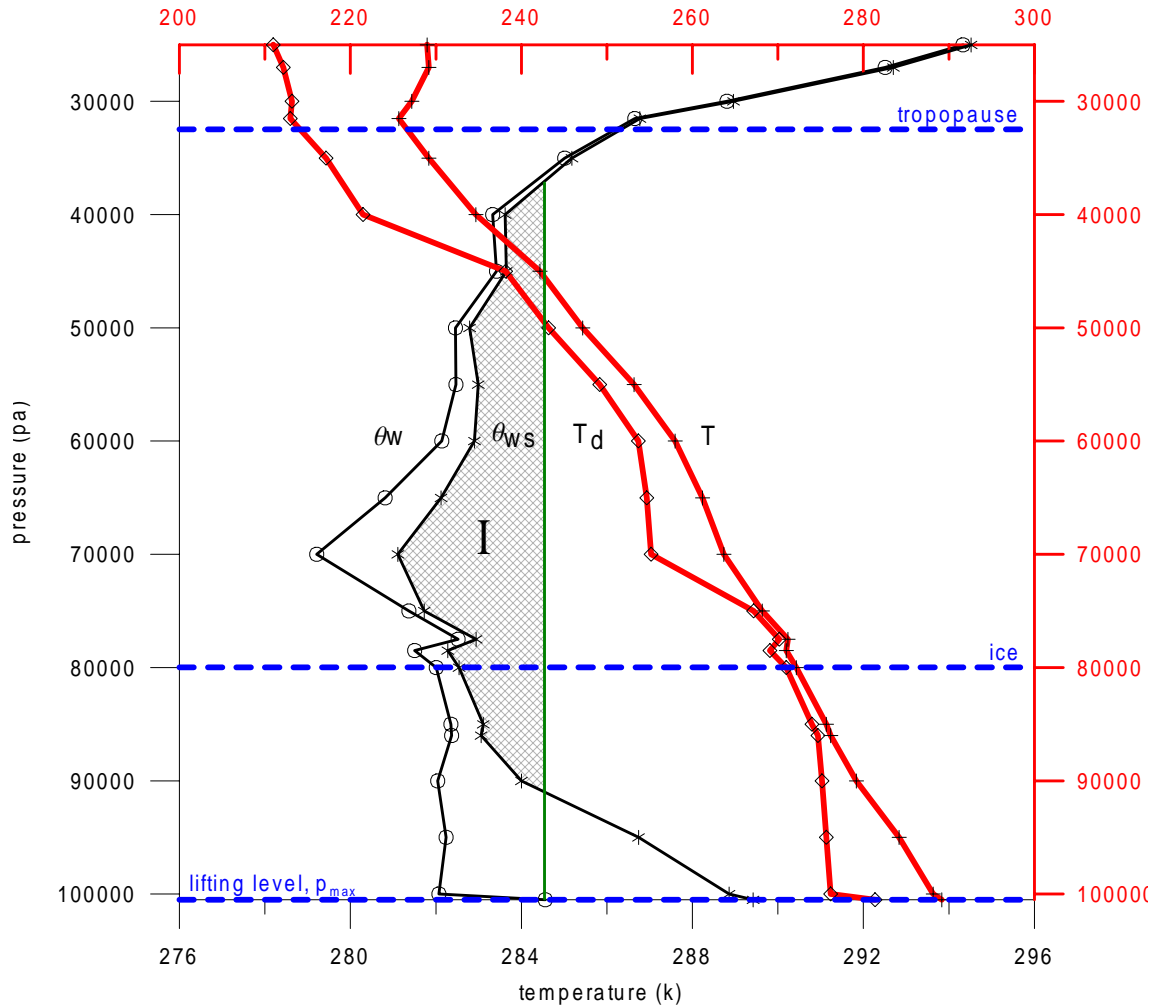


Figure 6: Profiles of temperature (T), dewpoint temperature (T_d), wet bulb potential temperature (θ_w) and wet bulb potential temperature at saturation (θ_{ws}). Vertical scale is pressure (hPa) and temperature scales (K) at bottom and top are for wet bulb potential temperature and temperature, respectively. Dashed lines show pressure at lifting level (p_{max}), freezing level (ice) and tropopause level. Shaded area I corresponds to I_{max} in equation (2).

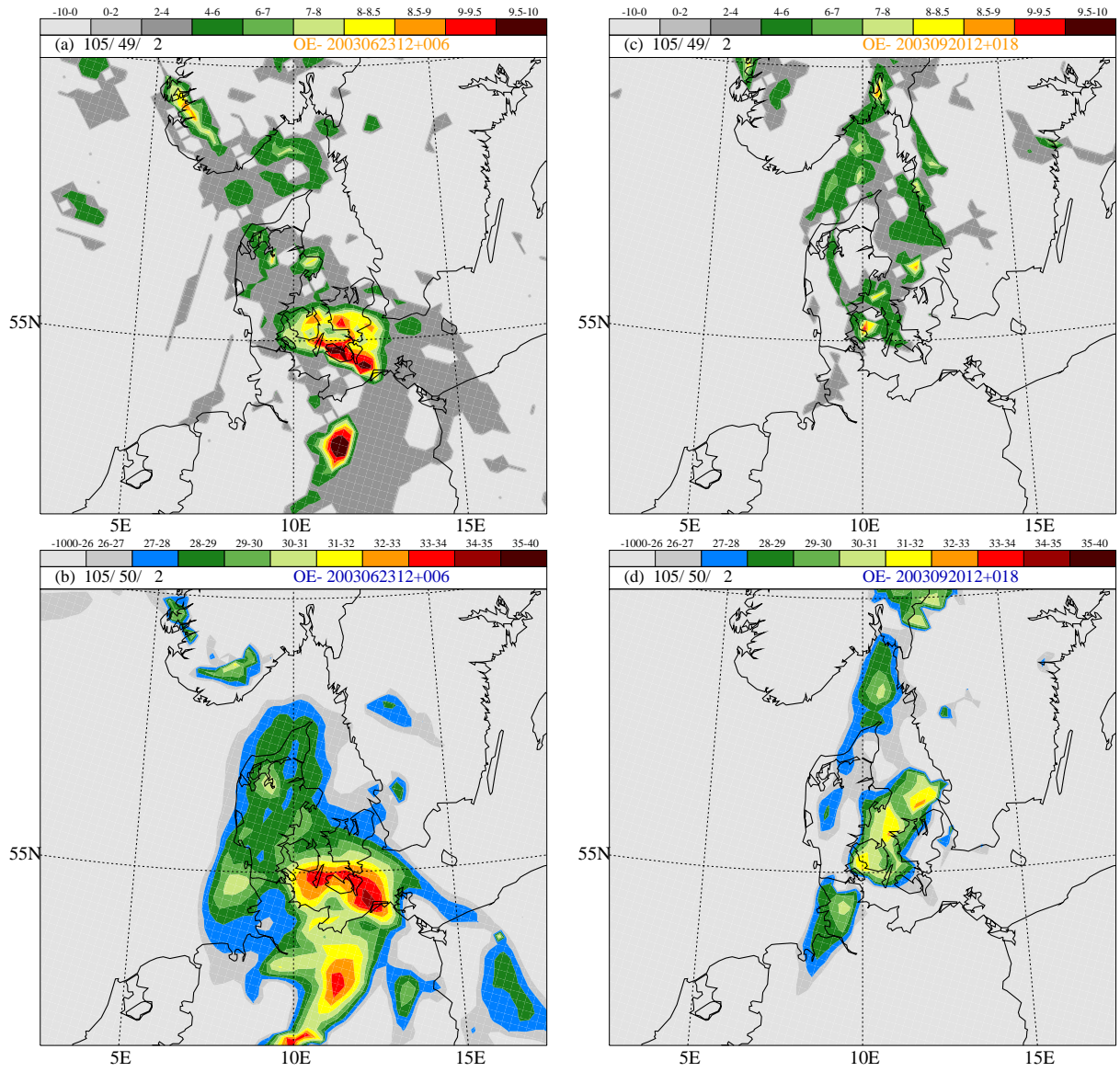
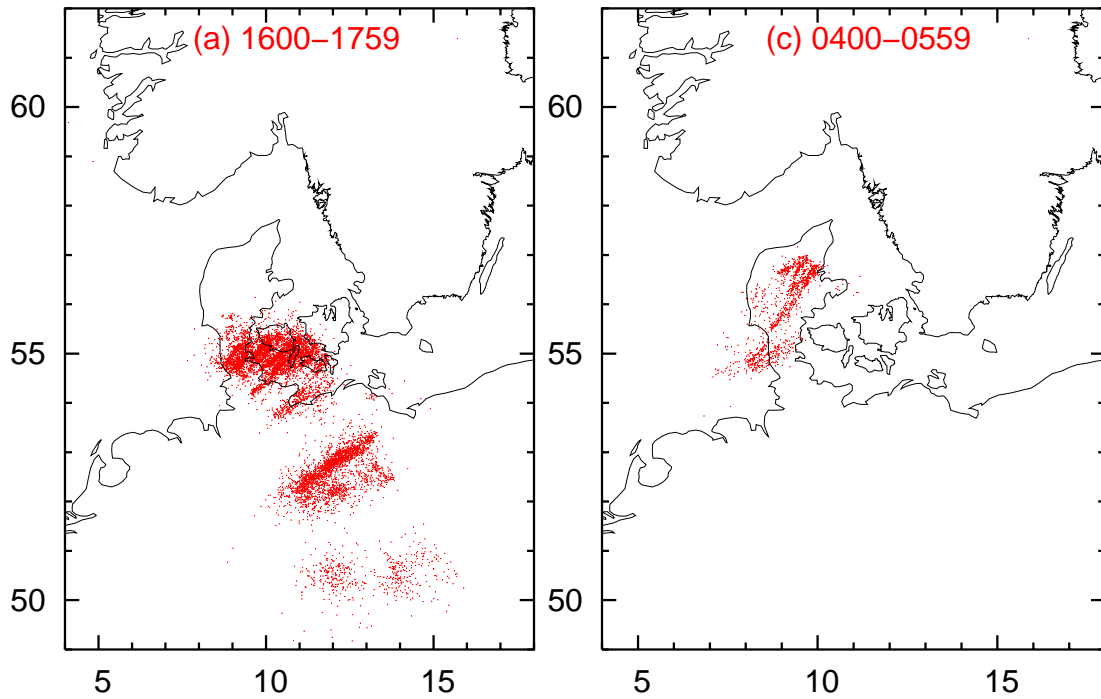


Figure 7: Same as Figure 3, but with a detailed view over Denmark.

Lightening data on June 23 2003

Lightening data on September 21 2003



Lightening data on June 23 2003

Lightening data on September 21 2003

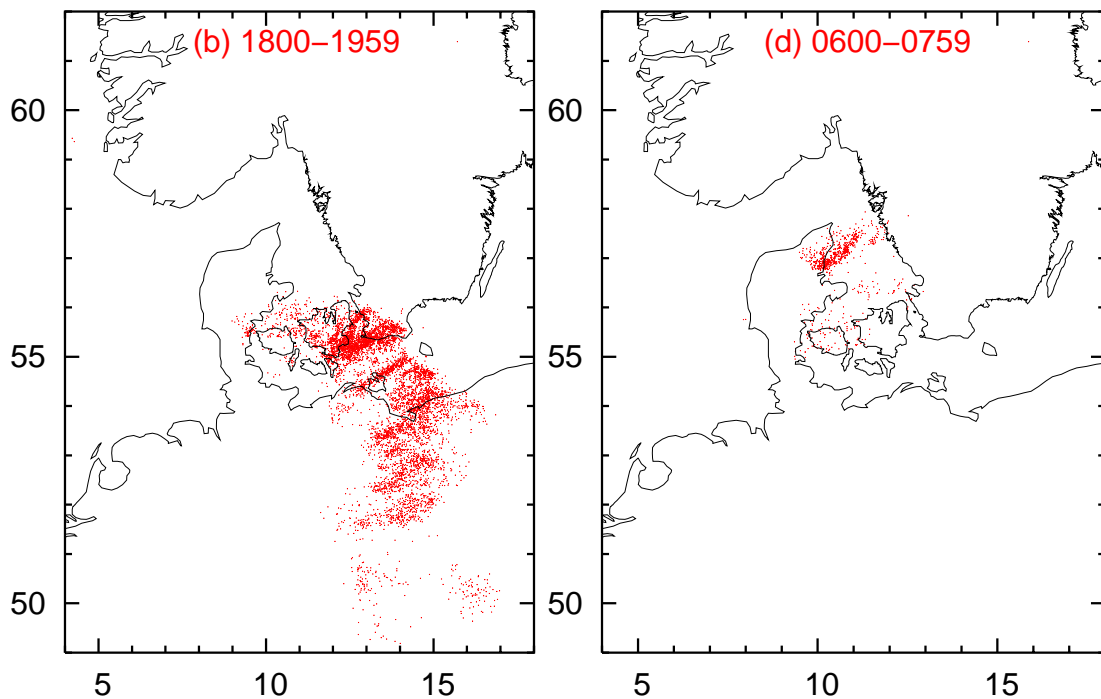


Figure 8: Lightening data from Denmark. Left: 16 to 18 and 18 to 20 UTC 23 June 2003. Right: 04 to 06 and 06 to 08 UTC 21 September 2003.

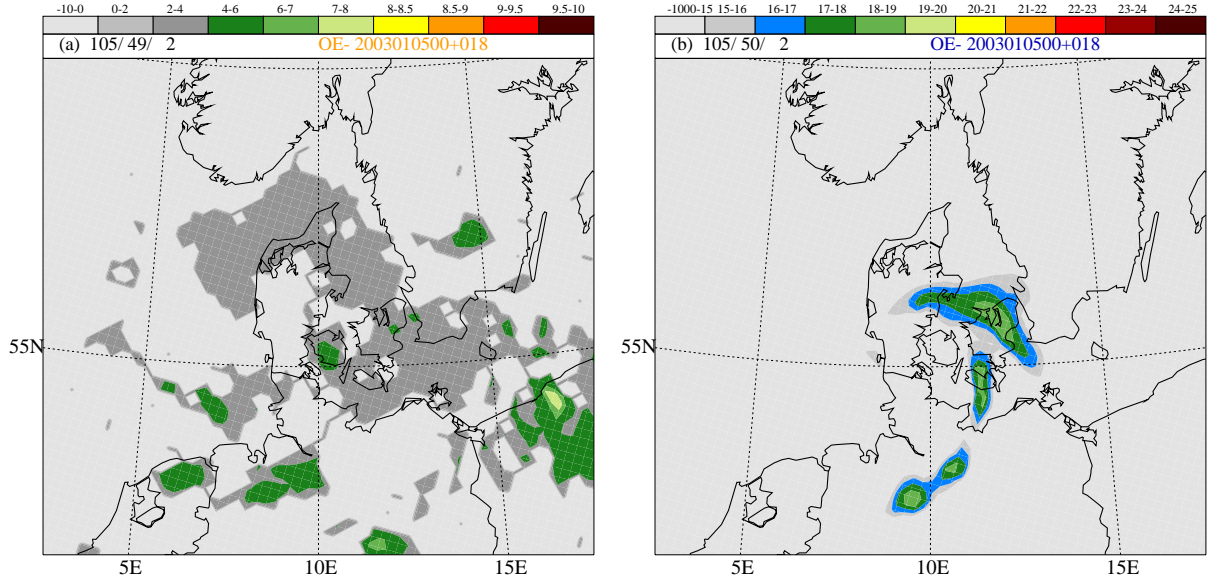


Figure 9: Left: θ_w -index and right: K-index for a 18 hour DMI-HIRLAM-E forecast valid 18 UTC 5 January 2003. Note that the K-index scale is different from the scale in Figure 3 and Figure 5.

$$I_{max}(p_b) = - \int_{p_{max}}^{p_b} (\theta_w^p(p_{max}) - \theta_{ws}^e(p)) \cdot dp \leq 0. \quad (3)$$

If (3) is not satisfied for $p_{max} \geq p \geq p_T$ it is assumed that p_b is the first pressure level above p_T . The θ_w -index, I_{θ_w} , is finally calculated by the (heuristic) equation

$$I_{\theta_w} = \exp\left(-d_1 \cdot (z_i + d_1)^{-1}\right) \quad (4)$$

if both I_{max} and $\Delta\theta_{wmax}$ are positive and by

$$I_{\theta_w} = \exp(z_i - 1.) \quad (5)$$

if $I_{max} \leq 0$. Note that I_{θ_w} takes values in the interval $[0,1]$. In equations (4) and (5)

$$z_i = \Delta\theta_{wmax} \cdot I_{max} \cdot (s_a \cdot s_b)^{\frac{1}{2}} / (\Delta p \cdot \Delta T^2) \quad (6)$$

is a nondimensional parameter. In (6) $\Delta\theta_{wmax}$ is the the maximum of the difference $\theta_w^p(p_{max}) - \theta_{ws}^e(p)$ in parcel lifting from p_{max} , $\Delta p = 500$ hPa and $\Delta T = 0.2$ K are tentative scaling constants and $s_a = (p_{max} - \min(p_{max}, p_{ice}) + 0.1\Delta p) / \Delta p$ and $s_b = (p_{max} - p_b) / (p_s - p_T)$. In the s_a -expression p_{ice} is the pressure at temperature $T_{ice} = 268.16$ K at which ice crystals are likely to be present in the convective cloud. The value $T_{ice} = 268.16$ K is tentative. In reality T_{ice} varies with a number of parameters, for example cloud top temperature, cloud type, cloud age and geographical location. For given values of I_{max} and $\Delta\theta_{wmax}$ the factor $(s_a \cdot s_b)^{0.5}$ has the effect of increasing the probability of thunderstorms if the depth of the convective cloud (measured by

$p_{max} - p_b$) is large and if the depth of the cloud fraction with temperature above T_{ice} (measured by $p_{max} - \min(p_{max}, p_{ice}) + 0.1\Delta p$) is large. Presently $d_1 = 0.1$. Equation (6) also shows that the nondimensional parameter z_i is proportional to $\Delta\theta_{wmax}$ and I_{max} . If $\Delta\theta_{wmax} < 0$, I_{θ_w} is set to -1.0. This occurs if the troposphere is stable with respect to parcel lifting from pressure levels below p_c . Note that this procedure implies that the θ_w -index does not account for moist symmetric instability, which occasionally occurs in regions with rapid extratropical cyclogenesis (e.g. Dixon et al., 2002). The same holds for the K-index. Note also that the θ_w -index, as defined by (4) and (5), has values in the interval $[0,1]$. Values at the upper and lower end of the interval means high and low probability of thunderstorms, respectively. The θ_w -index has a stronger physical foundation than the simpler K-index, but this does not automatically guarantee a better performance of the θ_w -index. The K-index has dimension of temperature and can take values in a broad interval. If the index is below 26 K thunderstorms are considered unlikely. A K-index above 30 K is often interpreted as high probability of thunderstorms.

3. Case studies

Three case studies are performed with the purpose of illustrating the behavior of the θ_w -index and compare its performance with the performance of the simpler K-index. The latter index is defined: $K_i = T_{850} - T_{500} + T_{d850} - T_0 - (T_{700} - T_{d700})$. Here T_d is dew point temperature and the subscript numbers denote pressure level in hPa. K_i usually gives good guidance in thunderstorm forecasting, although it has problems in mountain regions and generally (according to our experience) has a tendency to display too large areas with a high risk of thunderstorms. The first case is from 23 June 2003 (C1), the second case is from 21 September 2003 (C2) and the third case is from 5 January 2003 (C3), i.e. in the middle, towards the end and outside the thunderstorm season in northern Europe. Figure 3 shows the θ_w -index and the K-index for the entire integration domain (including the boundary zone) of DMI-HIRLAM-E in C1 and C2.

Figure 3 shows a tendency for extensive regions with high values of the θ_w -index in sections of the boundary zone with inflowing air. The reason for this behavior has not been investigated. So far the hypothesis is that the problem mainly is generated by differences in the moisture fields of the nested models DMI-HIRLAM-G and DMI-HIRLAM-E. The K-index is less sensitive to humidity, and according to Figure 3 there is no sign of any significant deterioration of the K-index in the boundary zone. Indirectly, this supports the hypothesis given above.

Comparison of the stability indices with observations and satellite cloud images indicates that the K-index tends to display too large regions with a high probability of thunderstorms, particularly in mountain areas. Figure 3c is a typical example. In comparison, the regions with high probability of thunderstorms shown by the θ_w -index are narrow and usually more discontinuous in space.

At any given time thunderstorms tend to occur in narrow regions and often also discontinuous in space. This makes verification of the instability indices against synop observations very uncertain because of the large distances (in some regions several hundred kilometers) between the observations. Over sea the observations are so few that thunderstorms rarely are reported. Verification of the instability indices over sea, based

on surface observations, is therefore of little value.

Despite of the coarse resolution of surface observations over land the resolution is high enough to show a significant correlation between areas with observed thunderstorms and areas with predicted high values of the instability indices. Figure 3 and Figure 5 show that the correlation over land is good for both stability indices, but as previously noted, with a tendency for the K-index to have too large areas with high instability, in particular in mountain areas (Spain and Tunisia in Figure 3). Both in C1 and C2 the θ_w -index in these areas appears to be in better agreement with the available observations. For the shown cases high values of I_{θ_w} over sea covers larger areas than corresponding high values of the K-index. In C2 lightning observations (Figure 5b) off the west coast of Portugal show that thunderstorms are present in the area. The best guidance appears here to be given by I_{θ_w} (Figure 3c).

Occasionally the θ_w -index shows clear frontal structures as in Figure 3c. The frontal structures are also seen in the K-index if the interval from 10 to 25 K is resolved in a color spectrum similar to the interval 26 to 40 K in Figure 3d. Note also that the location of the band with high values of I_{θ_w} is in good agreement with the satellite cloud image in Figure 4. It is not unlikely that thunderstorms develop along the sharp cold front southeast of Iceland and in the spiral cloud band southwest of Ireland. Unfortunately, no observations are available for verification. An interesting feature of the cold front southeast of Iceland is the sharp downward slope of the tropopause along the polar air side of the front. The slope is clearly shown in Figure 1d. It is most likely a manifestation of a tropopause fold on the cyclonic shear side of the polar jet.

Lightening data is available over Denmark. This type of information has a high space and temporal resolution and is therefore valuable in a verification of the instability indices. For verification purposes an enlargement of Figure 3 with focus over Denmark is shown in Figure 7. In Figure 8 lightening data is shown for the cases C1 and C2, covering a time window of minus and plus 2 hours around the verification times of the forecasts in Figure 7. In C1 both instability indices have high values (i.e. high probability of thunderstorms) in the regions with large numbers of lightening detections. Prior to 18 UTC the lightening detections within the area shown by figure 7 are concentrated in two regions. A similar separation is also seen in the instability indices in Figure 8a and b. After 18 UTC the lightening detections show that the thunderstorms develop more continuously in space along a cold front of a small-scale extratropical cyclone entering its mature stage. The latter is revealed in a detailed study of the case C1 in Nielsen, 2003.

Apparently both the θ_w -index and the K-index show areas with "false alarms", i.e. spots with relatively high values of the indices where no lightening has been detected. However, one should keep in mind that the instability indices are based on parcel lifting. If the dynamical lifting is absent the instability indices may be relatively high without any thunderstorm development.

In case C2 both instability indices give warnings about thunderstorms, although the areas with high instability values (Figure 7c and d) are slightly out of phase with the lightening detections (Figure 8c and d). Note that both the number of lightening detections and the values of the instability indices are smaller than in C1.

In case C3 the θ_w -index (Figure 9a) shows spots with moderately high values (0.6 to 0.8), giving indication of a weak possibility of thunderstorms. The K-index is nowhere

above 19K (Figure 9 b), indicating no possibility of thunderstorms. Actually, at 18 UTC one report of thunderstorms was given and one lightning was detected (at the North Sea coast of Germany).

4. Discussion and conclusion

The present report describes the θ_w -index, which is a generalized instability index, displaying areas within the model domain with a high probability of thunderstorms. The θ_w -index is based on calculation of vertical profiles of θ_w and θ_{ws} . Fast converging iteration algorithms were developed for calculation of these profiles. The θ_w -index also required an estimate of tropopause pressure. The latter was calculated by log-linear interpolation on the basis of temperature gradients in four consecutive layers in a $\ln p$ - T plane. In selected case studies the estimated tropopause pressure was shown to be in good agreement with observations or, if only few or no observations were available, in good qualitative agreement with satellite cloud images.

The performance of the θ_w -index has been compared with the performance of the simpler K-index for the same case studies. In mountain regions evidence for a better performance of the generalized instability index was noted. Over land without mountains the case studies indicated that the two indices performed equally good, except for a clear tendency of the K-index to show too extensive regions of high values. Due to a general lack of observations over sea it was not possible to make a verification of the indices there. However, it was noted that the θ_w -index tended to display larger areas with high values than the K-index. In one of the cases reports about thunderstorms over sea were in favor of the θ_w -index.

Only extended-period verification (one year as a minimum) of the instability indices can give reliable statistics about their performance. A good spatio-temporal resolution of the observations is essential. This requires use of other data sources than synop observations. One such source is lightning data, which has high spatio-temporal resolution and large areal coverage. It is the plan to utilize lightning data from the Danish area in a verification of the instability indices and report about the results for 2004 at the end of the year. It is desirable (and the next goal) to extend the verification to a European or larger scale, but this requires as a minimum that lightning data from the European area becomes easily accessible.

Appendix A. The T_w profile

The air is cooled if liquid water or ice evaporates at constant pressure into unsaturated air. If cooling is allowed to continue until the air is saturated, the temperature of the air has dropped to the wet bulb temperature T_w . This temperature can be measured by ventilating a thermometer whose sensing bulb is kept wet by a piece of damp cloth. Since the process is isobaric, the total specific enthalpy (or moist specific enthalpy) of the air-water system is kept constant. The total specific enthalpy k is (Emanuel, 1994)

$$k = (c_{pd} + r_t c_l)T + L_v r. \quad (7)$$

Here c_{pd} and c_l is the heat capacity of dry air and liquid water at constant pressure, respectively, r_t is the total water content, r and T is the mixing ratio and temperature of the ambient air, respectively, and L_v is the latent heat of vaporization. The enthalpy of the ambient air and the air cooled to saturation by evaporation, as described above, is $(c_{pd} + r_t c_l)T + L_v(T)r$ and $(c_{pd} + r_t c_l)T_w + L_v(T_w)r^*(T_w)$, respectively. The total water content r_t at saturation must be the sum of the mixing ratio r of the ambient air and the amount of water that has been evaporated into the air. At saturation we therefore have $r_t = r^*(T_w)$, where $r^*(T_w)$ is the saturation mixing ratio at temperature T_w . Since the total specific enthalpy is conserved in the considered process we then have

$$[c_{pd} + r^*(T_w)c_l] \cdot (T - T_w) = L_v(T_w)r^*(T_w) - L_v(T)r(T). \quad (8)$$

This is an implicit relation for T_w given T and r , which must be solved by iteration. For this purpose we define

$$F(T_w) = (T - T_w) \cdot (c_{pd} + r^*(T_w)c_l) - L_v(r^*(T_w) - r(T)), \quad (9)$$

and

$$x = \frac{e^*(T_w)}{p}, \quad (10)$$

where $e^*(T_w)$ is the saturation vapor pressure at T_w . Note that the variation of L_v with temperature has been neglected in (9). In the iteration procedure we substitute T_w by $T_w + \delta T_w$ in (9) and repeat this step until $F(T_w + \delta T_w) < \epsilon_0$, where ϵ_0 is a specified small number ($\ll 1$). The increment δT_w is obtained from a linear approximation to

$$F(T_w + \delta T_w) = [T - (T_w - \delta T_w)] \cdot (c_{pd} + r^*(T_w + \delta T_w)c_l) - L_v \cdot (r^*(T_w + \delta T_w) - r) = 0. \quad (11)$$

We use Tetens's formula for $e^*(T_w)$, i.e.

$$e^*(T_w) = a_1 \cdot \exp\left(\frac{T_w - T_0}{T_w - a_3} \cdot a_2\right). \quad (12)$$

In (12) $a_1=610.78$ Pa is the water vapor saturation pressure at the water freezing temperature $T_0 = 273.16$ K, and a_2 and a_3 are constants changing value at T_0 . For $T < T_0$, $a_2=21.875$ and $a_3=7.66$, and for $T \geq T_0$, $a_2=17.269$ and $a_3=35.86$.

$$r^*(T_w) = \epsilon \frac{e^*(T_w)}{p - e^*(T_w)}; \epsilon = 0.622 \quad (13)$$

and (10) we have

$$r^*(T_w + \delta T_w) = \epsilon \frac{x + \delta x}{1 - (x + \delta x)} \approx r^*(T_w) + \epsilon \frac{\delta x}{(1 - x)^2}. \quad (14)$$

A relation between the increments of δx and δT_w is obtained from Tetens's formula (12). From

$$\ln(e^*(T_w)) = \ln(a_1) + \frac{T_w - T_0}{T_w - a_3} \cdot a_2 = \ln(p \cdot x) \quad (15)$$

and

$$\ln(e^{*(T_w)} + \delta T_w) = \ln(a_1) + \frac{T_w - T_0 + \delta T_w}{T_w - a_3 + \delta T_w} \cdot a_2 = \ln(p \cdot x(1 + \frac{\delta x}{x})) \quad (16)$$

we get

$$\frac{T_w - T_0 + \delta T_w}{T_w - a_3 + \delta T_w} \cdot a_2 - \frac{T_w - T_0}{T_w - a_3} \cdot a_2 = \ln(1 + \frac{\delta x}{x}). \quad (17)$$

If the left hand side (lhs) of (17) is approximated by

$$\text{lhs} \approx \delta T_w a_2 (T_0 - a_3) (T_w - a_3)^{-2} \quad (18)$$

and the right hand side (rhs) of (17) is approximated by

$$\text{rhs} \approx \frac{\delta x}{x} \quad (19)$$

we obtain

$$\delta T_w = \frac{\delta x (T_w - a_3)^2}{x a_2 (T_0 - a_3)}. \quad (20)$$

Substitution of (14) and (20) into (11) yields

$$\delta T_w = F(T_w) (f_1 + f_2)^{-1} \quad (21)$$

where

$$f_1 = [a_2 (T_0 - a_2) (T_w - a_3)^{-2} r^*(T_w) (1 - x)^{-1} c_l (\frac{L_v}{c_l} + T_w - T)] \quad (22)$$

and

$$f_2 = c_{pd} + r^*(T_w) c_l. \quad (23)$$

As a first guess of T_w we use

$$T_w = wT + (1 - w)T_d, \quad (24)$$

where T_d is the dew point temperature and the weight w is defined as

$$w = \min \left(\max \left(\frac{210}{T}, 0.5 \right), 0.98 \right). \quad (25)$$

The iteration procedure usually requires 1 to 3 iterations for convergence with an accuracy $\epsilon_0 = 10^{-3}$.

Appendix B. The θ_w profile

Calculation of this profile is based on Bolton's formula for pseudo-equivalent potential temperature θ_{ep} (Bolton, 1980; Emanuel, 1994), which is

$$\theta_{ep} = T \left(\frac{p_0}{p} \right)^{\kappa(1-0.28r)} \cdot \exp \left(r(1+0.81r) \left(\frac{3376}{T^*} - 2.54 \right) \right). \quad (26)$$

In (26) $\kappa=R_d/c_p=0.2854$, $p_0=1000$ hPa and T^* is approximated by

$$T^* = \frac{2840}{3.5 \cdot \ln(T) - \ln(e) - 4.805} + 55. \quad (27)$$

T^* is the saturation temperature and e is the partial vapor pressure. For a given temperature, pressure and mixing ratio of an air parcel, T^* is the temperature the parcel attains in adiabatic expansion to saturation (occurring at the saturation pressure p^*). The wet bulb potential temperature of an air parcel (with θ_{ep} determined by (26)) is obtained by moving the air parcel pseudo-adiabatically (i.e. with conservation of θ_{ep}) to the reference pressure $p_0 = 1000$ hPa. From (26) we obtain

$$\theta_{ep} = \theta_w \cdot \exp \left(r'(1+0.81r') \left(\frac{3376}{\theta_w} - 2.54 \right) \right), \quad (28)$$

where $r' = r^*(T = \theta_w, p_0)$. Equation (28) is solved by iteration. Before the iteration is done we take the logarithm of (28) and define

$$B(\theta_w) = \ln \left(\frac{\theta_{ep}}{\theta_w} \right) - r'(1+0.81r') \left(\frac{3376}{\theta_w} - 2.54 \right) = 0. \quad (29)$$

The iteration is done by substituting θ_w with $\theta_w + \delta\theta_w$ in (29) and repeating this step until $B(\theta_w + \delta\theta_w) < \epsilon_0$. A new value of the increment $\delta\theta_w$ is obtained from a linearization of $B(\theta_w + \delta\theta_w)=0$. The linearization leads to

$$\delta\theta_w = \frac{B(\theta_w)}{(\theta_w^{-1} + g_1g_2 - g_3)}, \quad (30)$$

where

$$g_1 = \epsilon \cdot x_0 \cdot a_2(T_0 - a_3)(1 - x_0)^{-1} \cdot (\theta_w - a_3)^{-2}, \quad (31)$$

$$g_2 = \frac{3376}{\theta_w} - 2.54 + 1.62\epsilon x_0(1 - x_0)^{-1}, \quad (32)$$

$$g_3 = 3376\epsilon x_0(1 - x_0)^{-1}(1 + 0.81\epsilon x_0(1 - x_0)^{-1})\theta_w^{-2} \quad (33)$$

and $x_0 = e^*(\theta_w)p_0^{-1}$. As a first guess of θ_w we use $\theta_w = T_w\pi(p)^{-1}$, where $\pi(p) = (pp_0^{-1})^\alpha$ and $\alpha = \kappa(\exp(pp_0^{-1} + \delta))^{-1}$. For $p > 250$ hPa and $p \leq 250$ hPa we use $\delta=0.05$ and 0.20 , respectively. The iteration procedure usually requires 1 to 3 iterations for convergence with an accuracy $\epsilon_0 < 0.001$. It was found by experimentation that the convergence was practically equally fast by applying a first guess based on the simpler estimate of T_w in (24) instead of using the more accurate T_w obtained from (11). For

this reason the generalized instability index does not contain the iterative calculation of T_w described in Appendix A. However, this appendix has been retained in the present report for the sake of completeness and because an accurate T_w field may be useful in other applications.

Appendix C. The θ_{ws} profile

The vertical profile of θ_{ws} is calculated similar to θ_w . The pseudo-equivalent potential temperature at saturation θ_{eps} is calculated from (26) with $T^* = T$, $p^* = p$ and $r = r^*(T^*, p^*)$, i.e.

$$\theta_{eps} = T \left(\frac{p_0}{p} \right)^{\kappa(1-0.28r^*)} \cdot \exp \left(r^*(1 + 0.81r^*) \left(\frac{3376}{T} - 2.54 \right) \right). \quad (34)$$

Similarly

$$\theta_{eps} = \theta_{ws} \cdot \exp \left(r'(1 + 0.81r') \left(\frac{3376}{\theta_{ws}} - 2.54 \right) \right), \quad (35)$$

where $r' = r^*(\theta_{ws}, p_0)$. Again this equation must be solved by iteration. This is done by using (28) to (33) with θ_w , θ_{ep} , $\delta\theta_w$ and x replaced by θ_{ws} , θ_{eps} , $\delta\theta_{ws}$ and $x_s = e^*(\theta_{ws})p^{-1}$, respectively. As a first guess of θ_{ws} we use $\theta_{ws} = T(pp_0^{-1})^{-\kappa}$ if $p = p_s$, otherwise $\theta_{ws} = \theta_w + ((T - T_w)r^*r^{-1})^{1/2}$ with T_w given by (24).

Appendix D. List of symbols

- $a_1=610.78$ Pa, water vapor pressure at $T = T_0$
- $a_2=21.875$ if $T < T_0$, else $a_2=17.269$
- $a_3=7.66$ if $T < T_0$, else $a_3=35.86$
- $\alpha = \kappa(\exp(pp_0^{-1} + \delta))^{-1}$
- $a_p=0.6$, constant in expression for "critical" pressure p_c
- $c = \partial T / \partial \ln p$: Vertical temperature gradient on $\ln p$ -T diagram (K)
- $c_0 = 38.2$: Gradient of a vertical temperature profile on a $\ln p$ -T diagram (K)
- c_l : Specific heat capacity of liquid water at constant pressure ($\text{Jkg}^{-1}\text{K}^{-1}$)
- c_{pd} : Specific heat capacity of dry air at constant pressure ($\text{Jkg}^{-1}\text{K}^{-1}$)
- $d_1 = 0.1$: Constant in the θ_w -index.
- $\delta=0.05$ if $p > 250$ hPa, else $\delta=0.20$
- $\Delta p = 500$: Scaling pressure (hPa)
- $\Delta T = 0.2$: Scaling temperature (K)
- $\Delta\theta_{wmax}$: Maximum of difference $\theta_w^p(p_{max}) - \theta_{ws}^e(p)$

- e : Water vapor pressure (Pa)
- e^* : Water vapor pressure at saturation (Pa)
- $\epsilon=0.61$
- ϵ_0 : Accuracy of iteration
- $f_1 = [a_2(T_0 - a_2)(T_w - a_3)^{-2}r^*(T_w)(1 - x)^{-1}c_l(\frac{L_w}{c_l} + T_w - T)]$
- $f_2 = c_{pd} + r^*(T_w)c_l$
- $g_1 = \epsilon \cdot x_0 \cdot a_2(T_0 - a_3)(1 - x_0)^{-1} \cdot (\theta_w - a_3)^{-2}$
- $g_2 = \frac{3376}{\theta_w} - 2.54 + 1.62\epsilon x_0(1 - x_0)^{-1}$
- $g_3 = 3376\epsilon x_0(1 - x_0)^{-1}(1 + 0.81\epsilon x_0(1 - x_0)^{-1})\theta_w^{-2}$
- $I_i = \int_{p_i}^p (\theta_w^p(p_i) - \theta_{ws}^e(p')) \cdot dp'$ (K Pa)
- $I_{imax} = \int_{p_i}^{p_{imax}} (\theta_w^p(p_i) - \theta_{ws}^e(p')) \cdot dp'$ (K Pa)
- I_{imax} : Maximum of I_{imax} , $i=1,\dots,k$
- $I_{\theta_w} = \exp(-d_1 \cdot z_i^{-1})$: θ_w -index
- k : Specific enthalpy (Jkg⁻¹)
- $K_i = T_{850} - T_{500} + T_{d850} - T_0 - (T_{700} - T_{d700})$: K-index (K)
- p : Pressure (Pa)
- $p_0 = 10^5$: Reference pressure (Pa)
- p_b : First pressure level where $I_{imax} \leq 0$ (Pa)
- p_c : "Critical" pressure in parcel lifting (Pa)
- p_i : Lifting pressure level i (Pa)
- p_{max} : Lifting pressure level where $I = I_{imax}$ (Pa)
- p_{imax} : Level with maximum value of $I_i(p) = \int_{p_i}^p (\theta_w^p(p_i) - \theta_{ws}^e(p')) \cdot dp'$ (Pa)
- p_s : Surface pressure (Pa)
- p^* : Saturation pressure (Pa)
- p_T : Pressure at the tropopause (Pa)
- R_d : Gas constant of dry air (Jkg⁻¹K⁻¹)
- r : Mixing ratio (kgkg⁻¹)

- r_t : Total water content (kgkg^{-1})
- r^* : Saturation mixing ratio (kgkg^{-1})
- $s_a = (p_{max} - \min(p_{max}, p_{ice}) + 0.1)\Delta p/\Delta p$
- $s_b = (p_{max} - p_b)/(p_s - p_T)$
- T : Absolute temperature (K)
- $T_0=273.16$: Freezing temperature (K)
- T_d : Dew point temperature (K)
- $T_{ice}=268.16$: Temperature at which ice crystals are present in clouds (K)
- T_w : Wet bulb temperature (K)
- T^* : Saturation temperature (K)
- θ_w : Wet bulb potential temperature (K)
- θ_{ws} : Saturation wet bulb potential temperature (K)
- θ_{ep} : Pseudo-equivalent potential temperature (K)
- θ_{eps} : Saturation pseudo-equivalent potential temperature (K)
- w : Weight function
- $x = e^*(T_w)p^{-1}$
- $x_0 = e^*(\theta_w)p_0^{-1}$
- $x_s = e^*(\theta_{ws})p^{-1}$
- $z_i = \Delta\theta_{wmax} \cdot I_{max} \cdot (s_a \cdot s_b)^{\frac{1}{2}}/(\Delta p \cdot \Delta T^2)$

References

- Bluestein, H. B. (1993). *Synoptic-Dynamic Meteorology in Midlatitudes, Volume 2: Observations and Theory of Weather Systems*. Oxford University Press.
- Bolton, H.. (1980). *The computation of equivalent potential temperature*. Mon. Wea. Rev.,108:1046–1053.
- Dixon, R., Browning, K., and Shutts, G. (2002). The relation of moist symmetric instability and upper-level potential-vorticity anomalies to the observed evolution of cloud heads. *Quart. J. Roy. Meteor. Soc.*, 128:839–860.
- Emanuel, K. A. (1994). *Atmospheric convection*. Oxford University Press.
- Hess, S. L. (1966). *Introduction to theoretical meteorology*. Holt, Rinehart and Winston.
- Nielsen, N. W. (2003). Uvejret Skt. Hans Aften 2003. *Vejret*, 96:10–21.

DANISH METEOROLOGICAL INSTITUTE

Scientific Reports

Scientific reports from the Danish Meteorological Institute cover a variety of geophysical fields, i.e. meteorology (including climatology), oceanography, subjects on air and sea pollution, geomagnetism, solar-terrestrial physics, and physics of the middle and upper atmosphere.

Reports in the series within the last five years:

No. 99-1

Henrik Feddersen: Project on prediction of climate variations on seasonal to interannual timescales (PROVOST) EU contract ENVA4-CT95-0109: DMI contribution to the final report: Statistical analysis and post-processing of uncoupled PROVOST simulations

No. 99-2

Wilhelm May: A time-slice experiment with the ECHAM4 A-GCM at high resolution: the experimental design and the assessment of climate change as compared to a greenhouse gas experiment with ECHAM4/OPYC at low resolution

No. 99-3

Niels Larsen et al.: European stratospheric monitoring stations in the Arctic II: CEC Environment and Climate Programme Contract ENV4-CT95-0136. DMI Contributions to the project

No. 99-4

Alexander Baklanov: Parameterisation of the deposition processes and radioactive decay: a review and some preliminary results with the DERMA model

No. 99-5

Mette Dahl Mortensen: Non-linear high resolution inversion of radio occultation data

No. 99-6

Stig Syndergaard: Retrieval analysis and methodologies in atmospheric limb sounding using the GNSS radio occultation technique

No. 99-7

Jun She, Jacob Woge Nielsen: Operational wave forecasts over the Baltic and North Sea

No. 99-8

Henrik Feddersen: Monthly temperature forecasts for Denmark - statistical or dynamical?

No. 99-9

P. Thejll, K. Lassen: Solar forcing of the Northern hemisphere air temperature: new data

No. 99-10

Torben Stockflet Jørgensen, Aksel Walløe Hansen: Comment on "Variation of cosmic ray flux and global coverage - a missing link in solar-climate relationships" by Henrik Svensmark and Eigel Friis-Christensen

No. 99-11

Mette Dahl Meincke: Inversion methods for atmospheric profiling with GPS occultations

No. 99-12

Hans-Henrik Benzon; Laust Olsen; Per Høeg: Simulations of current density measurements with a Faraday Current Meter and a magnetometer

No. 00-01

Per Høeg; G. Leppelmeier: ACE - Atmosphere Climate Experiment

No. 00-02

Per Høeg: FACE-IT: Field-Aligned Current Experiment in the Ionosphere and Thermosphere

No. 00-03

Allan Gross: Surface ozone and tropospheric chemistry with applications to regional air quality modeling. PhD thesis

No. 00-04

Henrik Vedel: Conversion of WGS84 geometric heights to NWP model HIRLAM geopotential heights

No. 00-05

Jérôme Chenevez: Advection experiments with DMI-Hirlam-Tracer

No. 00-06

Niels Larsen: Polar stratospheric clouds microphysical and optical models

No. 00-07

Alix Rasmussen: "Uncertainty of meteorological parameters from DMI-HIRLAM"

No. 00-08

A.L. Morozova: Solar activity and Earth's weather. Effect of the forced atmospheric transparency changes on the troposphere temperature profile studied with atmospheric models

No. 00-09

Niels Larsen, Bjørn M. Knudsen, Michael Gauss, Giovanni Pitari: Effects from high-speed civil traffic aircraft emissions on polar stratospheric clouds

No. 00-10

Søren Andersen: Evaluation of SSM/I sea ice algorithms for use in the SAF on ocean and sea ice, July 2000

No. 00-11

Claus Petersen, Niels Woetmann Nielsen: Diagnosis of visibility in DMI-HIRLAM

No. 00-12

Erik Buch: A monograph on the physical oceanography of the Greenland waters

No. 00-13

M. Steffensen: Stability indices as indicators of lightning and thunder

No. 00-14

Bjarne Amstrup, Kristian S. Mogensen, Xiang-Yu Huang: Use of GPS observations in an optimum interpolation based data assimilation system

No. 00-15

Mads Hvid Nielsen: Dynamisk beskrivelse og hydrografisk klassifikation af den jyske kyststrøm

No. 00-16

Kristian S. Mogensen, Jess U. Jørgensen, Bjarne Amstrup, Xiaohua Yang and Xiang-Yu Huang: Towards an operational implementation of HIRLAM 3D-VAR at DMI

No. 00-17

Sattler, Kai; Huang, Xiang-Yu: Structure function characteristics for 2 meter temperature and relative humidity in different horizontal resolutions

No. 00-18

Niels Larsen, Ib Steen Mikkelsen, Bjørn M. Knudsen m.fl.: In-situ analysis of aerosols and gases in the polar stratosphere. A contribution to THESEO. Environment and climate research programme. Contract no. ENV4-CT97-0523. Final report

No. 00-19

Amstrup, Bjarne: EUCOS observing system experiments with the DMI HIRLAM optimum interpolation analysis and forecasting system

No. 01-01

V.O. Papitashvili, L.I. Gromova, V.A. Popov and O. Rasmussen: Northern polar cap magnetic activity index PCN: Effective area, universal time, seasonal, and solar cycle variations

No. 01-02

M.E. Gorbunov: Radioholographic methods for processing radio occultation data in multipath regions

No. 01-03

Niels Woetmann Nielsen; Claus Petersen: Calculation of wind gusts in DMI-HIRLAM

No. 01-04

Vladimir Penenko; Alexander Baklanov: Methods of sensitivity theory and inverse modeling for estimation of source parameter and risk/vulnerability areas

No. 01-05

Sergej Zilitinkevich; Alexander Baklanov; Jutta Rost; Ann-Sofi Smedman, Vasilij Lykosov and Pierluigi Calanca: Diagnostic and prognostic equations for the depth of the stably stratified Ekman boundary layer

No. 01-06

Bjarne Amstrup: Impact of ATOVS AMSU-A radiance data in the DMI-HIRLAM 3D-Var analysis and forecasting system

No. 01-07

Sergej Zilitinkevich; Alexander Baklanov: Calculation of the height of stable boundary layers in operational models

No. 01-08

Vibeke Huess: Sea level variations in the North Sea – from tide gauges, altimetry and modelling

No. 01-09

Alexander Baklanov and Alexander Mahura: Atmospheric transport pathways, vulnerability and possible accidental consequences from nuclear risk sites: methodology for probabilistic atmospheric studies

No. 02-01

Bent Hansen Sass and Claus Petersen: Short range atmospheric forecasts using a nudging procedure to combine analyses of cloud and precipitation with a numerical forecast model

No. 02-02

Erik Buch: Present oceanographic conditions in Greenland waters

No. 02-03

Bjørn M. Knudsen, Signe B. Andersen and Allan Gross: Contribution of the Danish Meteorological Institute to the final report of SAMMOA. CEC contract EVK2-1999-00315: Spring-to.-autumn measurements and modelling of ozone and active species

No. 02-04

Nicolai Kliem: Numerical ocean and sea ice modelling: the area around Cape Farewell (Ph.D. thesis)

No. 02-05

Niels Woetmann Nielsen: The structure and dynamics of the atmospheric boundary layer

No. 02-06

Arne Skov Jensen, Hans-Henrik Benzon and Martin S. Lohmann: A new high resolution method for processing radio occultation data

No. 02-07

Per Høeg and Gottfried Kirchengast: ACE+: Atmosphere and Climate Explorer

No. 02-08

Rashpal Gill: SAR surface cover classification using distribution matching

No. 02-09

Kai Sattler, Jun She, Bent Hansen Sass, Leif Laursen, Lars Landberg, Morten Nielsen og Henning S. Christensen: Enhanced description of the wind climate in Denmark for determination of wind resources: final report for 1363/00-0020: Supported by the Danish Energy Authority

No. 02-10

Michael E. Gorbunov and Kent B. Lauritsen: Canonical transform methods for radio occultation data

No. 02-11

Kent B. Lauritsen and Martin S. Lohmann: Unfolding of radio occultation multipath behavior using phase models

No. 02-12

Rashpal Gill: SAR ice classification using fuzzy screening method

No. 02-13

Kai Sattler: Precipitation hindcasts of historical flood events

No. 02-14

Tina Christensen: Energetic electron precipitation studied by atmospheric x-rays

No. 02-15

Alexander Mahura and Alexander Baklanov: Probabilistic analysis of atmospheric transport patterns from nuclear risk sites in Euro-Arctic Region

No. 02-16

A. Baklanov, A. Mahura, J.H. Sørensen, O. Rigina, R. Bergman: Methodology for risk analysis based on atmospheric dispersion modelling from nuclear risk sites

No. 02-17

A. Mahura, A. Baklanov, J.H. Sørensen, F. Parker, F. Novikov K. Brown, K. Compton: Probabilistic analysis of atmospheric transport and deposition patterns from nuclear risk sites in russian far east

No. 03-01

Hans-Henrik Benzon, Alan Steen Nielsen, Laust Olsen: An atmospheric wave optics propagator, theory and applications

No. 03-02

A.S. Jensen, M.S. Lohmann, H.-H. Benzon and A.S. Nielsen: Geometrical optics phase matching of radio occultation signals

No. 03-03

Bjarne Amstrup, Niels Woetmann Nielsen and Bent Hansen Sass: DMI-HIRLAM parallel tests with upstream and centered difference advection of the moisture variables for a summer and winter period in 2002

No. 03-04

Alexander Mahura, Dan Jaffe and Joyce Harris: Identification of sources and long term trends for pollutants in the Arctic using isentropic trajectory analysis

No. 03-05

Jakob Grove-Rasmussen: Atmospheric Water Vapour Detection using Satellite GPS Profiling

No. 03-06

Bjarne Amstrup: Impact of NOAA16 and NOAA17 ATOVS AMSU-A radiance data in the DMI-HIRLAM 3D-VAR analysis and forecasting system - January and February 2003

No. 03-07

Kai Sattler and Henrik Feddersen: An European Flood Forecasting System EFFS. Treatment of uncertainties in the prediction of heavy rainfall using different ensemble approaches with DMI-HIRLAM

No. 03-08

Peter Thejll and Torben Schmith: Limitations on regression analysis due to serially correlated residuals: Application to climate reconstruction from proxies

No. 03-09

Peter Stauning, Hermann Lühr, Pascale Ultré-Guéraud, John LaBrecque, Michael Purucker, Fritz Primdahl, John L. Jørgensen, Freddy Christiansen, Per Høeg, Kent B. Lauritsen: OIST-4 Proceedings. 4th Oersted International Science Team Conference. Copenhagen 23-27 September 2002

No. 03-10

Niels Woetmann Nielsen: A note on the sea surface momentum roughness length.

No. 03-11

Niels Woetmann Nielsen: Quasigeostrophic interpretation of extratropical cyclogenesis

No. 03-12

Alexander Baklanov: FUMAPEX – project kick-off meeting and first progress report. Integrated systems for forecasting urban meteorology, air pollution and population exposure, EVK4-CT-2002-00097

No. 03-13

Rasmus Tonboe, Søren Andersen, Leif Toudal: Anomalous winter sea ice backscatter and brightness temperatures

No. 03-14

Alexander Mahura, Alexander Baklanov, Jens Havskov Sørensen: Long-term probabilistic atmospheric transport and deposition patterns from nuclear risk sites in euro-arctic region. Arctic risk – project of the Nordic Arctic Research Programme (NARP)

No. 03-15

Alexander Mahura, Alexander Baklanov: Evaluation of source-receptor relationship for atmospheric pollutants using trajectory modelling and probability fields analysis

No. 03-16

Niels Woetmann Nielsen, Claus Petersen: A generalized thunderstorm index developed for DMI-HIRLAM